Pergamon

0301-9322(94)00093-X

*Int. J. Multiphase Flow* Vol. 21, No. 3, pp. 437–454, 1995

0301-9322/95 $9.50 + 0.00

# POST-DRYOUT DISPERSED FLOW IN CIRCULAR BENDS

M. J. WANG† and F. MAYINGER
Lehrstuhl A für Thermodynamik, Technische Universität München, 80290 München, Germany

*(Received 8 December 1993; in revised form 13 December 1994)*

**Abstract**—The effect of curvature on the post-dryout dispersed flow in 90-degree circular bends is investigated theoretically and experimentally. The theoretical study concentrates on two basic aspects of the flow, i.e. bulk vapor flow and droplet dynamics. The former is analyzed by solving the conservation equations of the vapor phase whereas the latter is studied by a Lagrangian droplet trajectory model considering both thermal and turbulence effects. The experimental study deals with phase distribution of the flow by measuring local liquid fraction with an impedance probe. The results indicate that the curvature induced centrifugal force and the secondary flow significantly change the behavior of droplet dynamics and phase distribution. Droplets in the vapor stream reveal a general trend of centrifugal migration towards the outside of the bend and may even impinge directly on the wall. The effects of the secondary flow and turbulent dispersion are found to bring about a better circumferential transportation of liquid. Depending on the heat transfer condition, two different patterns of phase distribution are found. The first associated with film boiling is mainly dominated by phase separation. The second connected with the rewetting phenomenon is governed firstly by phase separation and then phase redistribution in the form of liquid inward reversal.

*Key Words:* dispersed flow, post-dryout, droplet dynamics, phase distribution, bend

## 1. INTRODUCTION

Post-dryout dispersed flow is referred to as a typical flow pattern of convective film boiling, in which dispersed liquid droplets flow together with the continuous vapor in the heated channel beyond the dryout point. Because of its importance in cryogenic equipment, in steam generating units and during several stages of a hypothetical loss-of-coolant accident in nuclear reactor systems, post-dryout dispersed flow heat transfer has been under extensive study, especially in simple geometries (see reviews of Mayinger & Langner 1978; Mayinger 1982; Chen 1986). These studies indicate that far away from the dryout location, dispersed flow appears to be symmetric and heat transfer from the wall is dominated by vapor convection. With small lateral kinetic energy, droplets are usually kept out of the heated surface due to the Leidenfrost effect, thus acting only as a disturbing factor in the boundary layer. Consequently, their contribution to the wall heat transfer is of secondary importance. Lin *et al.* (1989) showed that droplet–wall interactions in dispersed flow contribute only a few percent to the total wall heat transfer.

In complex geometries like coils and bends, heat transfer of post-dryout dispersed flow may differ from that in simple channels because of the change of flow structure. According to the measurements of Cumo *et al.* (1972) and Lautenschlager (1988), heat transfer varies tremendously along the circumference of the tube: it improves remarkably on the outer wall away from the curvature center whereas it exhibits a different behavior on the inner wall depending on the flow conditions. This phenomenon, as qualitatively explained in their work, was attributed to the actions of the centrifugal force and the induced secondary flow associated with the curved channels (Berger *et al.* 1983). Due to limited information on the dispersed flow dynamics, previous analysis of the heat transfer mechanisms remained, in general, qualitative. Thus, it is the purpose of this paper to clarify the curvature effect on the fundamental aspects of the post-dryout dispersed flow, namely, bulk vapor flow, droplet dynamics and phase distribution, therefore providing a sounder basis of the heat transfer analysis.

†Present address: RUD. OTTO MEYER, Ladenmannbogen 12, 22339 Hamburg, Germany.

## 2. METHODOLOGY

### 2.1. Theoretical

In view of the nature of high vapor quality in post-dryout dispersed flow, bulk vapor fields and dynamics of individual droplets are two important aspects of the flow that determine the behavior of phase distribution and heat transfer. These two basic aspects are theoretically investigated in this paper.

As an approximation, the bulk vapor fields are numerically studied by solving the single-phase Eulerian conservation equations and the standard $k$–$\epsilon$ turbulence model together with the boundary conditions related to our two-phase experiment. The computations were carried out using the finite-difference code FLOW3D (Burns & Wilkes 1987) on a general non-orthogonal body-fitted grid in the Cartesian co-ordinate system. The hybrid differencing scheme was used for the convective term. The SIMPLEC algorithm was used for the pressure–velocity decoupling. A modified and three-dimensional version of the Rhie & Chow algorithm was used to overcome the problem of checkerboard oscillations usually associated with the use of non-staggered grids. The constants used in the $k$–$\epsilon$ turbulence model $C_\mu$, $C_1$, $C_2$, $\sigma_k$, $\sigma_1$ were set to be 0.09, 1.44, 1.92, 1.0 and 0.9, respectively. Standard wall functions, i.e. the log layers functions, were used near the walls. Numerical details are given in Wang (1993).

A Lagrangian droplet trajectory model was developed to study the dynamics of individual droplets in the superheated turbulent vapor stream. Some assumptions are employed in this model. One of them is the validity of the one-way coupling treatment, i.e. the presence of droplets does not modify the vapor flow and temperature fields. This simplification allows a direct introduction of the vapor fields from the numerical computation of the single-phase flow. Other assumptions include:

(1) Droplets remain spherical before and after impact on the wall.
(2) Interactions among droplets are not taken into account.
(3) Forces due to virtual mass, Basset history integral, etc. are neglected because of the high ratio of liquid to vapor density.
(4) Lift forces due to mean shear and droplet rotation are not considered due to the uncertainty in modeling when the droplet Reynolds number is larger than one (White 1986).
(5) Radiation heat transfer is small enough to be neglected here.

The path of an evaporating droplet can then be described by the following balance equations for force

$$\frac{\mathrm{d}(m_\mathrm{d} V_{\mathrm{d},i}\mathbf{e}_i)}{\mathrm{d}t} = (F_{\mathrm{D},i} + F_{\mathrm{b},i} + F_{\mathrm{t},i})\mathbf{e}_i \qquad [1]$$

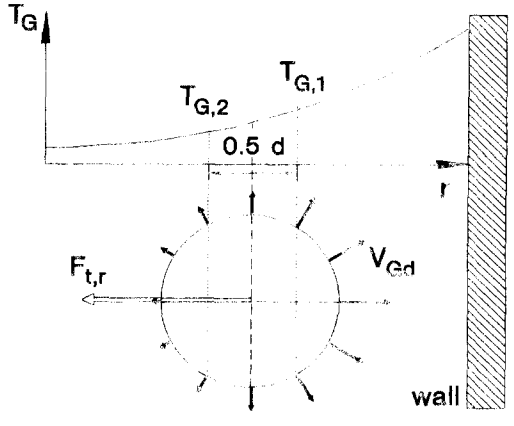


Figure 1. Schematic of the thermal repelling force.

and energy

$$h_{LG}\frac{dm_d}{dt} = -\dot{Q}_{Gd} \quad [2]$$

where $m_d$ is the mass of the droplet, $V_{d,i}$ is the droplet velocity component, $\mathbf{e}_i$ is the unit vector of the co-ordinate system, $F_{D,i}$, $F_{b,i}$, $F_{t,i}$ are the components of drag, buoyancy and thermal repelling force acting on the droplet, $h_{LG}$ is the latent heat and $\dot{Q}_{Gd}$ is the heat convection rate from superheated vapor to the droplet.

In [1], the drag force due to the slip between two phases is given by

$$F_{D,i} = \tfrac{1}{8}\pi d^2 c_D \rho_G |\mathbf{V}_G - \mathbf{V}_d|(V_{G,i} - V_{d,i}) \quad [3]$$

where $\mathbf{V}_G$ and $\mathbf{V}_d$ are the velocity vectors of the vapor and the droplet, $V_{G,i}$ is the velocity component of the vapor, $d$ is the droplet diameter, $c_D$ is the drag coefficient, determined by (Renksizbulut & Yuen 1983).

$$c_D = \frac{24}{Re_d}(1 + 0.2\,Re_d^{0.63})(1 + \mathbf{B})^{-0.2} \quad [4]$$

in which the droplet Reynolds number $Re_d$ is defined as

$$Re_d = \frac{\rho_G|\mathbf{V}_G - \mathbf{V}_d|d}{\mu_G} \quad [5]$$

and the Spalding number B is defined as

$$\mathbf{B} = \frac{h_G - h_{G,S}}{h_{LG}} \quad [6]$$

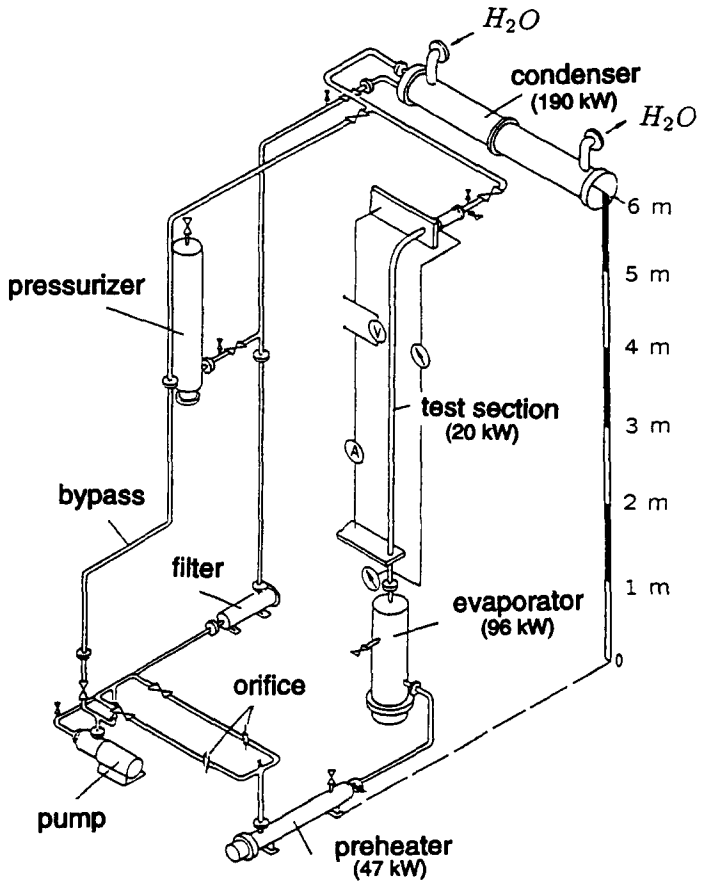


Figure 2. Sketch of the R12 experimental loop.

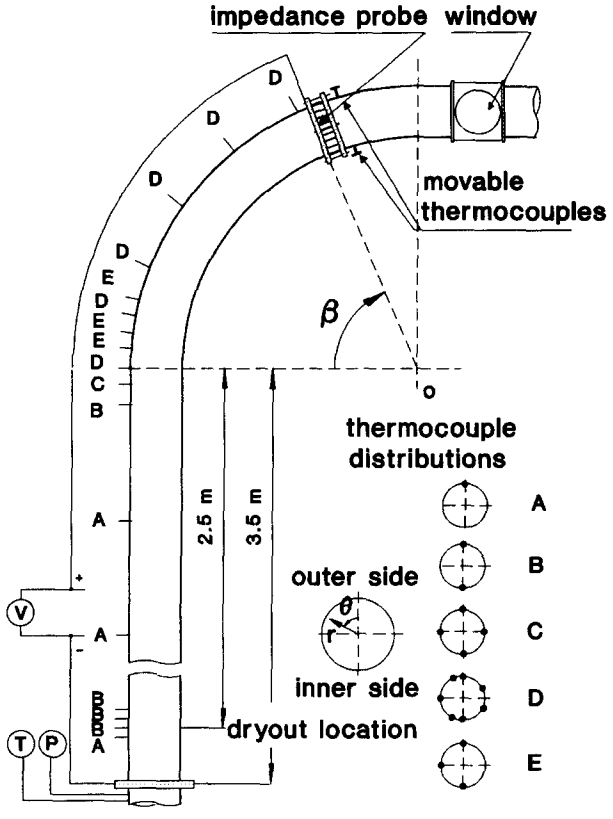


Figure 3. Layout of the test section.

Here $h_G$, $h_{G,S}$ are the vapor enthalpies corresponding to the superheating and saturation temperatures. The term $(1 + B)^{-0.2}$ in the drag correlation accounts for the reduction in drag due to the blowing effect of uniform evaporation.

The buoyancy is expressed as

$$F_{b,i} = \tfrac{1}{6}\pi d^3(\rho_L - \rho_G)g_i \qquad [7]$$

where $g_i$ is the gravitational acceleration in the $\mathbf{e}_i$ direction.

The thermal repelling force due to the non-uniform evaporation on the droplet surface is considered only in the radial direction following a similar approach of Ganic & Rohsenow (1979)

$$F_{t,r} = \iint_A V_{Gd,r}(\rho_G \mathbf{V}_{Gd}\,d\mathbf{A}) = \frac{\pi d^2 \alpha_{Gd}^2}{4h_{LG}^2\rho_G}[(T_{G,2} - T_S)^2 - (T_{G,1} - T_S)^2] \qquad [8]$$

where $\mathbf{V}_{Gd}$ is the vapor velocity leaving from the droplet surface $d\mathbf{A}$, $T_{G,1}$, $T_{G,2}$ are the vapor temperatures at the centers of the front and the rear part of the droplet in the direction towards the wall (see figure 1) and $\alpha_{Gd}$ is the convective heat transfer coefficient between the vapor and the droplet, determined by [10].

The term $\dot{Q}_{Gd}$ on the RHS of the [2] is expressed as

$$\dot{Q}_{Gd} = \pi d^2 \alpha_{Gd}(T_G - T_S) \qquad [9]$$

where the coefficient $\alpha_{Gd}$ is calculated according to Renksizbulut & Yuen (1983)

$$\alpha_{Gd} = \frac{\lambda_{G,f}}{d}(2 + 0.57\,\mathrm{Re}_d^{0.5}\,\mathrm{Pr}_{G,f}^{0.33})(1 + B)^{-0.7} \qquad [10]$$

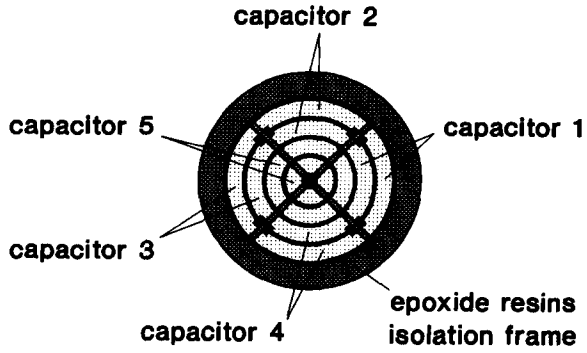


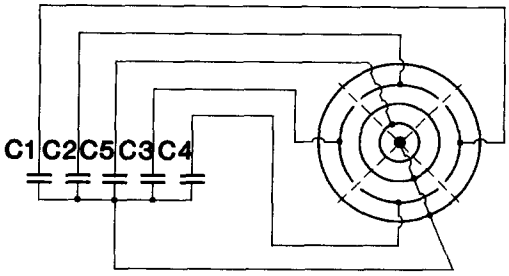


Figure 4. Structure of the impedance probe.

For flow analysis in the circular bend, it is convenient to use the toroidal co-ordinate system $(r, \theta, \beta)$. In this system (see figure 3), the derivative of the unit vector $\mathbf{e}_i$ with respect to time $t$ is a function of the Lagrangian velocity components and other unit vectors

$$\frac{d\mathbf{e}_r}{dt} = \frac{V_{d,\theta}}{r}\mathbf{e}_\theta + \frac{V_{d,\beta}\cos\theta}{R_c + r\cos\theta}\mathbf{e}_\beta \quad [11]$$

$$\frac{d\mathbf{e}_\theta}{dt} = -\frac{V_{d,\theta}}{r}\mathbf{e}_r - \frac{V_{d,\beta}\sin\theta}{R_c + r\cos\theta}\mathbf{e}_\beta \quad [12]$$

$$\frac{d\mathbf{e}_\beta}{dt} = -\frac{V_{d,\beta}\cos\theta}{R_c + r\cos\theta}\mathbf{e}_r + \frac{V_{d,\beta}\sin\theta}{R_c + r\cos\theta}\mathbf{e}_\theta \quad [13]$$

where $R_c$ is the bend radius. Introducing [11]–[13] into [1] and rearranging them leads to some additional terms, in which the combination

$$m_d\left(\frac{V_{d,\beta}^2\cos\theta}{R_c + r\cos\theta}\right)\mathbf{e}_r + m_d\left(\frac{V_{d,\beta}^2\sin\theta}{R_c + r\cos\theta}\right)\mathbf{e}_\theta$$

directing from the inner to the outer side of the curvature is conventionally called the centrifugal force.

Equations [1] and [2] for force and energy balance together with the equations for Lagrangian velocity components

$$\frac{dr}{dt} = V_{d,r} \quad [14]$$

$$\frac{d\theta}{dt} = \frac{V_{d,\theta}}{r} \quad [15]$$

$$\frac{d\beta}{dt} = \frac{V_{d,\beta}}{R_c + r\cos\theta} \quad [16]$$

are numerically integrated using the 4th-order Runge–Kutta algorithm.

The turbulence effect of the continuous vapor phase on the droplet motion is taken into account through a stochastic model, similar to that of Gosman & Ioannides (1981). It is assumed that the turbulence is made up of a collection of randomly directed eddies. These energy containing eddies are characterized by their length scale $l_e$, life time $t_e$ and rms velocity $V_e$

$$l_e = c_\mu^{0.75} k^{1.5} \quad [17]$$

$$t_e = 1.5^{0.5} c_\mu^{0.75} k \epsilon^{-1} \quad [18]$$

$$V_e = 1.5^{-0.5} k^{0.5} \quad [19]$$

where $k$, $\epsilon$ are the turbulent kinetic energy and dissipation rate of the vapor phase. The droplet during its stay in the flow domain is assumed to interact with a series of turbulent eddies which do not lose their identity during their lifetime. It remains in one eddy until the end of its lifetime unless it leaves the eddy. Then it begins to interact with a new one.

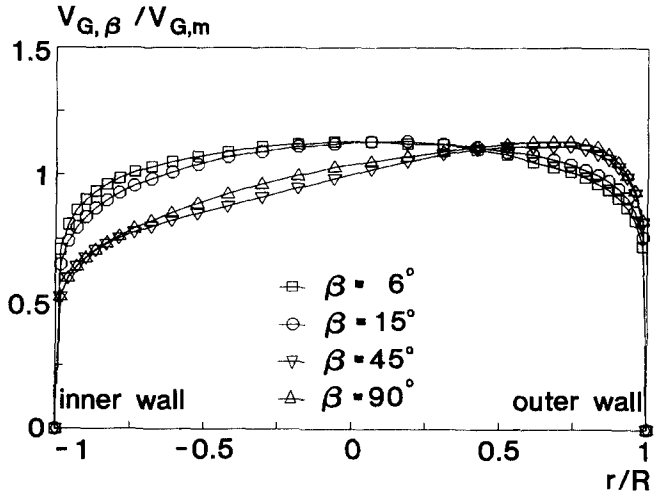


a) development of the primary flow

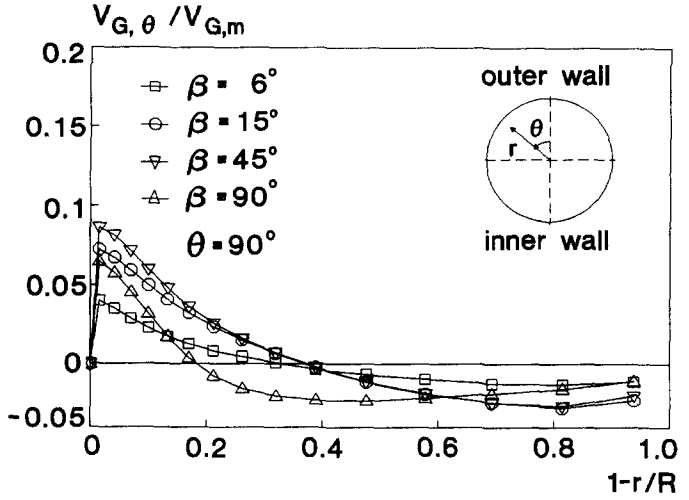


b) development of the secondary flow

Fig. 5(a) and (b). *Caption opposite.*

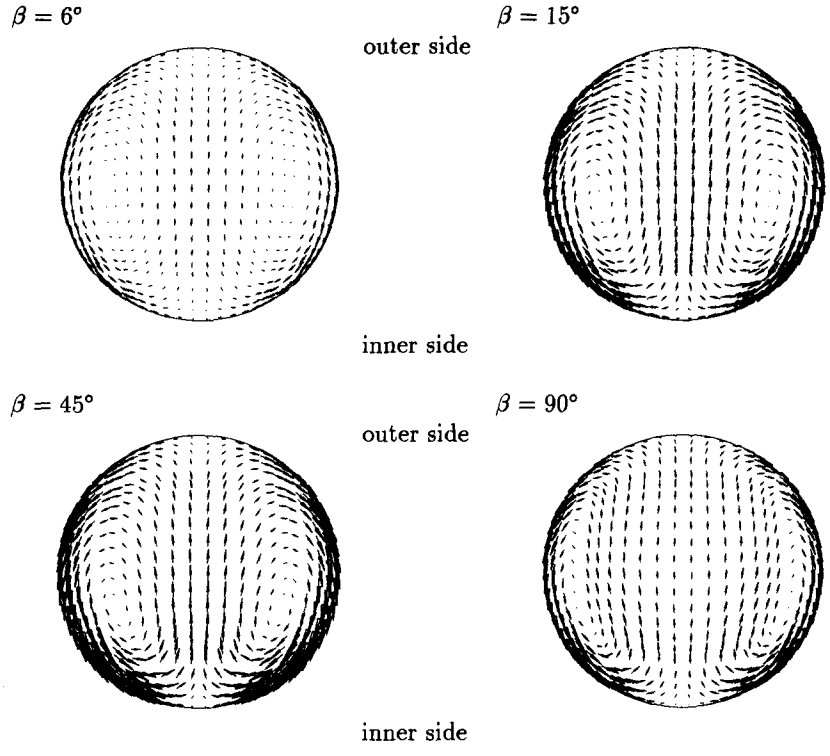


c) velocity vector field in the cross-section

Figure 5. Vapor flow structure at $R_c/R = 42$, $Re_G = 1.07 \times 10^6$.

The Reynolds decomposition of vapor velocities is used for the flow field

$$V_{G,i} = \bar{V}_{G,i} + V'_{G,i} \qquad [20]$$

where $\bar{V}_{G,i}$ is the time average velocity and $V'_{G,i}$ is the time fluctuating one, related with the rms velocity of the eddy

$$V'_{G,i} = \Psi_i V_e \qquad [21]$$

Here $\Psi_i$ is the normally distributed pseudorandom number. Including [17]–[21] into the balance equations, the effect of turbulent dispersion on the droplet motion is simulated.

Interactions of droplets with the hot wall (beyond the Leidenfrost temperature) are simulated following a graphical relation of Bolle & Moureau (1982) for the droplet impinging and rebounding Weber number. This relation can be mathematically expressed as

$$We_{re} = \begin{cases} We_{im} \\ 0.049 + 1.032We_{im} - 7.787 \times 10^{-2}We_{im}^2 + \\ 14.23 - 0.784We_{im} + 2.591 \times 10^{-2}We_{im}^2 - \\ 1.0 \end{cases}$$

$$\begin{array}{ll} We_{im} \leqslant 1 & \\ 2.59 \times 10^{-3}We_{im}^3 - 3.175 \times 10^{-4}We_{im}^4 & 1 < We_{im} < 30 \\ 3.88 \times 10^{-4}We_{im}^3 + 2.012 \times 10^{-6}We_{im}^4 & 30 \leqslant We_{im} \leqslant 80 \\ We_{im} > 80 & \end{array} \qquad [22]$$

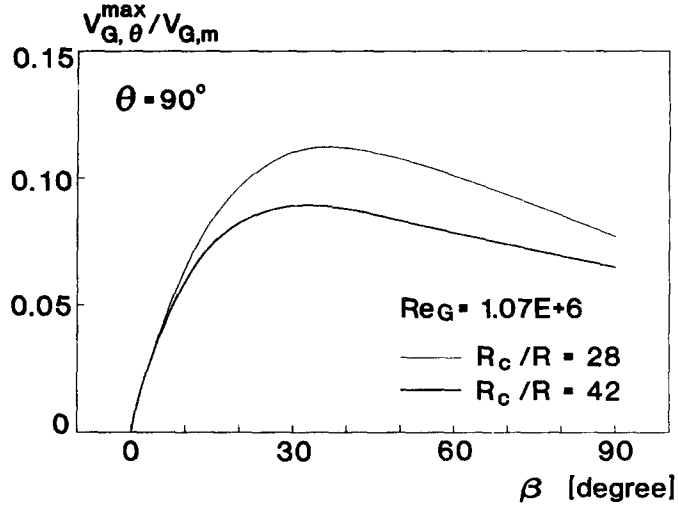


Figure 6. Influence of curvature ratio on the secondary flow.

where the Weber number, We, is defined as

$$\mathrm{We} = \frac{\rho_L V_{d,r}^2 d}{\sigma} \qquad [23]$$

According to Wachters & Westerling (1966), it is the normal velocity of the droplet that characterizes the droplet dynamics on the hot surface. Therefore only the velocity component in the radial direction $V_{d,r}$ is considered in the Weber number. The present model also considers droplet breakup on the wall. Based on the measurements of Wachters & Westerling, it is assumed that the breakup number of the impinging droplet is 1 for $\mathrm{We}_{im} < 30$, 2 for $30 \leqslant \mathrm{We}_{im} \leqslant 80$ and 10 for $\mathrm{We}_{im} > 80$.

### 2.2. *Experimental*

The effect of curvature on phase distribution of the post-dryout dispersed flow is studied experimentally. Figure 2 shows a schematic diagram of the two-phase flow test loop with the refrigerant Freon-12 (R12). Driven by a centrifugal pump, the refrigerant passed firstly through a control valve and an orifice flowmeter where mass flux was adjusted and measured. Then it entered a preheater in which the fluid was heated to a few Kelvins below the saturation level. A high quality

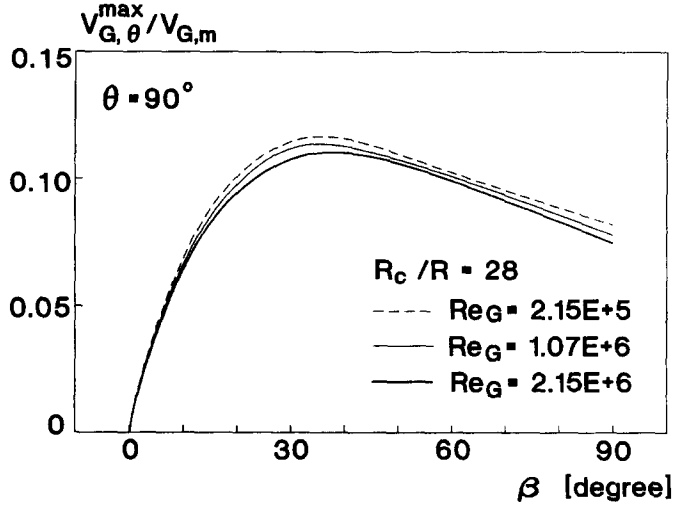


Figure 7. Influence of Reynolds number on the secondary flow.

two-phase flow was produced in an evaporator. The flow, in annular form, then entered a test section, Joule-heated by direct current. Through dryout of the flow, dispersed droplet flow was regulated to appear 2.5 m upstream of the bend inlet, a length sufficient for flow development. Extensive measurements were performed in the bend part of the test section. Further downstream, the two-phase mixture condensed in a water-cooled condenser. Finally, the refrigerant passed through a filter and flowed back to the pump inlet.

Figure 3 shows the layout of the test-section and the instrumentation. The stainless steel test-section had an inner diameter of 28.5 mm and a wall thickness of 2.6 mm. It consisted of a 3.5 m long vertical tube and a 90-degree bend. Due to bending, the tube had an ellipticity smaller than 4% and a maximum deviation in wall thickness of 4.6%.

Wall temperatures were measured by NiCr–Ni thermocouples of 0.5 mm diameter, spot welded on the outer surface of the tube (see figure 3 for distribution). Inner surface temperatures were then inferred from the Fourier conduction equation. As an approximation, average wall heat flux obtained from the heat generation over the whole test section was used in the calculation. Due to geometry deviation, resistance change, axial and circumferential conduction, local heat flux along the bend wall may differ from the average one. The first two factors have been estimated to give about 5% higher Joule-heating at the inner and 5% lower at the outer wall of the bend. The last factor, predominantly the circumferential conduction, however, produced an opposite effect. According to the analysis of Lautenschlager (1988), local heat flux is higher at the outer and lower at the inner wall with a deviation of about 10–15% average heat flux. In addition to the wall temperature measurement, local fluid temperatures in the bend were evaluated by two movable thermocouples installed right after the impedance probe.

A specially developed impedance probe was used to measure the local liquid fraction. By installing the probe at different angular positions, phase distribution along the bend was obtained. Figure 4 shows a sketch of the impedance probe. It consisted of concentric metal cylinders and cylindrical segments, isolated and supported by an epoxide resins frame. Electrical wiring between the metal components was done in such a way that five separate capacitors covering the different zones of the cross-section were constituted. Supplied with a 1 MHz high frequency voltage, these capacitors conveyed local capacitance signals through a Boonton digital capacitance meter, type 72BD, with a 0.15% full-range precision. The dielectric constant of the fluid was then deduced from the capacitance measurement, which may in turn be converted into liquid fraction under specific flow regimes. For dispersed droplet flow, the liquid fraction $1-\epsilon$ can be determined by the Maxwell correlation (Maxwell 1873)

$$1-\epsilon=\frac{e-e_G}{e+2e_G}\frac{e_L+2e_G}{e_L-e_G} \qquad [24]$$

where $e$, $e_L$, $e_G$ are the dielectric constants of two-phase mixture, pure liquid and pure gas, respectively.

Equation [24] has been proved to be reliable for void/liquid fraction measurement in dispersed flow, provided that the electric field between electrodes is homogeneous and the interval between dispersed particles is large compared to their dimensions. For example, Cimorelli & Evangelisti (1967) reported that the measuring error using the Maxwell correlation was much smaller than 0.02 in the void fraction range of 0–0.4 in bulk boiling. In the present experiment, however, it was sometimes difficult to maintain the Maxwell conditions, especially when a liquid film was formed on one of the electrodes as a result of intensive droplet deposition. Under this extreme case, the total capacitance measured is actually the resultant from two capacitors in series, i.e. one formed by the pure liquid film, and another by the dispersed mixture. The amount of error induced by using the Maxwell correlation is therefore proportional to the thickness of the liquid film. Wang (1993) revealed that such error remains small so long as the liquid film is thin, e.g. the relative error of the liquid fraction is only 9% when the liquid film occupies 10% of the total liquid. It can thus be concluded that the present measuring technique is appropriate for the study of high quality post-dryout dispersed flow.

The experiments covered a wide range of operational parameters: mass flux $G$, 400–1240 kg/m$^2$s; wall heat flux $\dot{q}_w$, 20–60 kW/m$^2$, bend-to-tube radius ratio (curvature ratio) $R_c/R$, 28, 42; reduced pressure $P/P_{cr}$, 9.5 bar/41.2 bar.

## 3. RESULTS AND DISCUSSION

### 3.1. Bulk vapor flow structure

The behavior of the bulk vapor flow along a 90-degree circular bend is demonstrated in figure 5. The results were obtained from the numerical computation for the Reynolds number of $1.07 \times 10^6$ and the curvature ratio $R_c/R$ of 42. Figure 5(a) shows profiles of the axial velocity $V_{G,\beta}$, non-dimensionalized by the mean inlet velocity $V_{G,m}$. It is seen that the bulk axial flow structure keeps nearly symmetric in the first 15 degrees from the bend inlet. Then acceleration in the region near the outer wall and deceleration near the inner wall become appreciable, and the velocity maximum is shifted towards the outer wall. It is noted here that the decrease of velocity near the inner wall is more significant than the increase near the outer wall. Figure 5(b) shows profiles of the secondary velocity $V_{G,\theta}$, non-dimensionalized by the mean inlet velocity, and figure 5(c) gives the development of the secondary flow represented by vector plots. It is revealed in these figures that the secondary flow in a double-vortex form increases very rapidly within the first 15 degrees, maintains a maximum region from about 15 to 45 degrees into the bend and then decreases slightly until the exit. In each cross-section, the secondary flow is much stronger in a narrow region close to the wall where droplet motion may be significantly affected.

In order to clarify its role to the dispersed flow behavior, secondary vapor flow is further studied for different Reynolds numbers (figure 6) and curvature ratios (figure 7). Here, profiles of the maximum secondary velocity $V_{G,\theta}^{max}$, non-dimensionalized by the mean inlet velocity are plotted as a function of the angular co-ordinate $\beta$. As seen from the figures, the secondary flow in terms of the non-dimensional velocity varies little by a ten-fold increase in the bulk Reynolds number. However, it changes significantly when increasing the curvature ratio from 28 to 42: the maximum velocity region shifts towards the bend inlet, with the magnitude decreasing from 11 to 9% of the mean velocity.

### 3.2. Behavior of droplet dynamics

*3.2.1. Droplet dynamics under turbulent dispersion.* Droplet dynamics in the turbulent vapor stream along a 90-degree circular bend are studied in figure 8. To concentrate our discussion on the flow dynamic features, heat transfer is not considered. This means that the flow considered here is in slight non-equilibrium or complete equilibrium state. For statistical analysis, trajectories of 1000 droplets were computed using the Lagrangian trajectory model introduced in section 2.1.

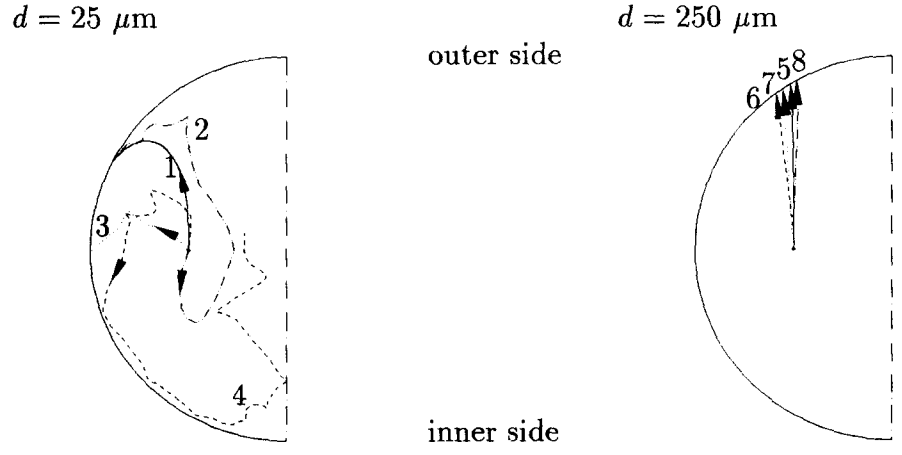


a) typical droplet trajectories

Fig. 8(a). *Caption opposite.*

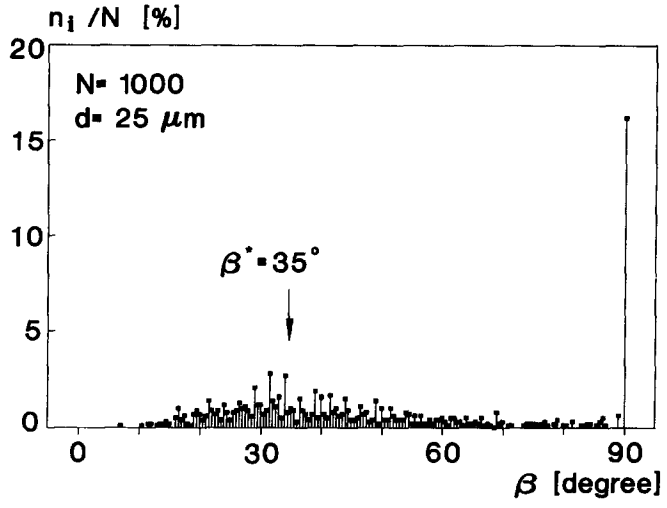


b) deposition histogram of small droplets

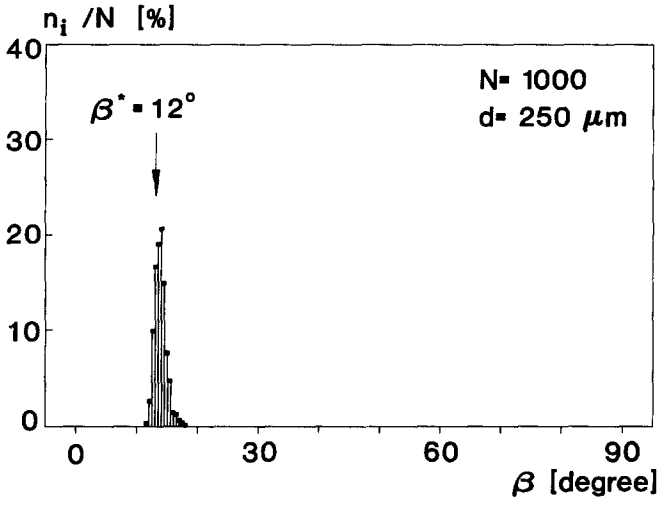


c) deposition histogram of large droplets

Figure 8. Droplet motion under turbulence dispersion: $R_c/R = 42$, $Re_G = 1.07 \times 10^6$.

These droplets were initially placed at a radial position of $0.5R$ at the bend inlet, with the same local velocity as the vapor phase. They were tracked from their release until they hit the tube surface.

Figure 8(a) shows typical trajectories of droplets with two different sizes. In the figure the broken lines represent the trajectories obtained with considering droplet–turbulent eddy interactions whereas the continuous lines are without turbulence dispersion. It can be seen that for small droplets with a diameter of 25 $\mu$m, their trajectories are influenced strongly by the secondary vapor flow (trajectory 1) and by the turbulent dispersion (trajectories 2–4). Both effects bring about a better circumfernetial transportation of droplets. On the contrary, large droplets with a diameter of 250 $\mu$m are insensitive to either the secondary flow or the turbulent dispersion (trajectories 5–8). Dominated by the centrifugal force, they move along straight lines towards the outer wall.

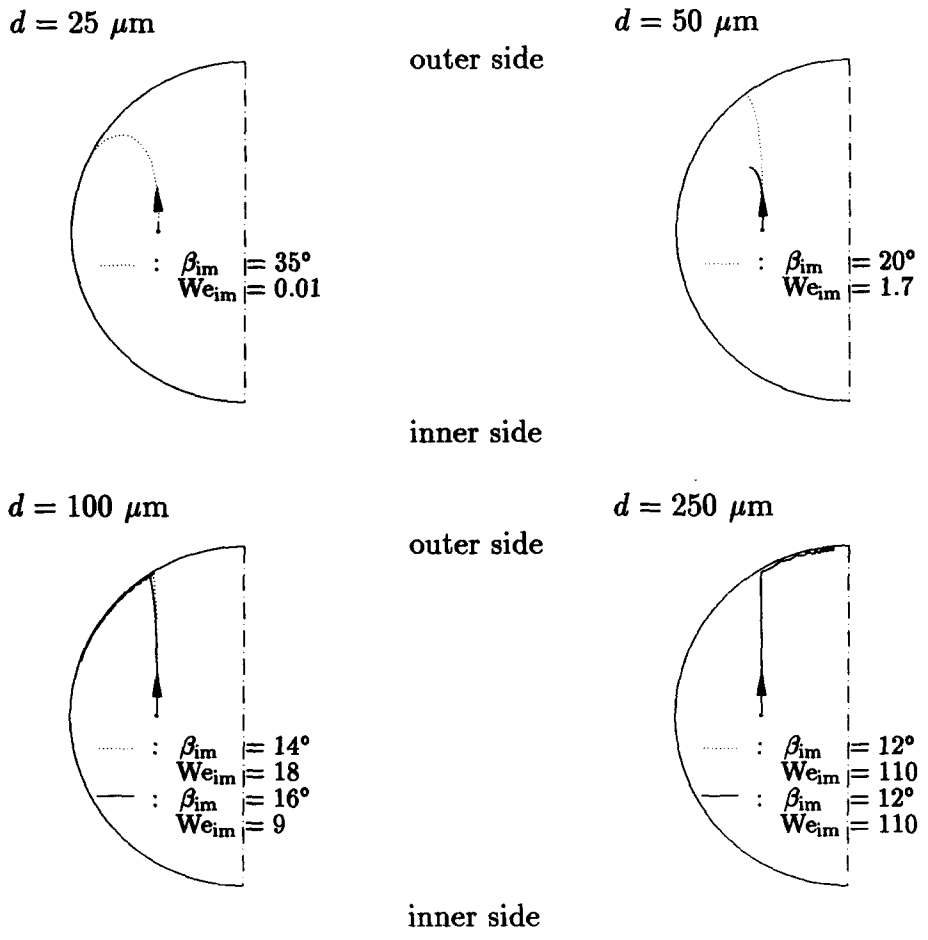


Figure 9. Droplet motion under thermal effect: $R_c/R = 42$, $Re_G = 1.07 \times 10^6$, $\dot{q}_w = 60\,kW/m^2$, $T_{G,0} - T_S = 80°C$.

Figure 8(b) and (c) illustrates the statistical nature of droplet deposition along the bend. Here $\beta^*$ is the droplet deposition position without turbulent effect. As seen from the figures, turbulence in a vapor stream leads to a scattered deposition of droplets of 25 $\mu$m. Some droplets, about 16% of the total, flow out of the bend without deposition whereas others deposit on the wall over a wide angular region. Increasing the droplet dimension, turbulent effect is significantly reduced. Nearly all droplets of 250 $\mu$m deposit in a narrow region centered by the path without turbulent effect.

*3.2.2. Droplet dynamics under thermal effect.* Including the thermal effect, droplet dynamics in the vapor stream and on the hot wall of the bend are studied in figure 9. To facilitate the discussion, turbulent dispersion on droplets is suppressed. The flow condition considered here is the same as in figure 8. In addition, a vapor superheating of 80°C is assumed at the bend inlet and the wall heat flux is set to be 60 kW/m$^2$ to simulate a high non-equilibrium condition.

In figure 9, droplet trajectories under thermal effect are represented by the continuous lines. Trajectories without considering the heat transfer are also displayed by the dotted lines for comparison. It is seen from the figure that small droplets from 25 to 50 $\mu$m evaporate quickly in the vapor stream which implies their weak contribution to the wall heat transfer. In terms of their trajectories, evaporating droplets are found to follow the paths of the secondary vapor flow more easily than those in equilibrium flows. For larger droplets over 100 $\mu$m, however, effects of evaporation and the secondary flow are less significant. The centrifugal force dominates the droplet motion in the bulk region, resulting in a direct droplet collision on the bend wall. It is noticed that although the wall temperature here is sufficiently high to produce a large temperature gradient near

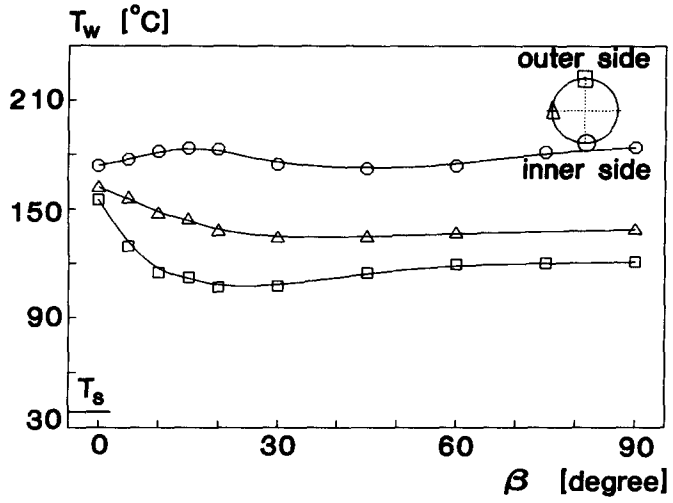


a) measurement of wall temperature

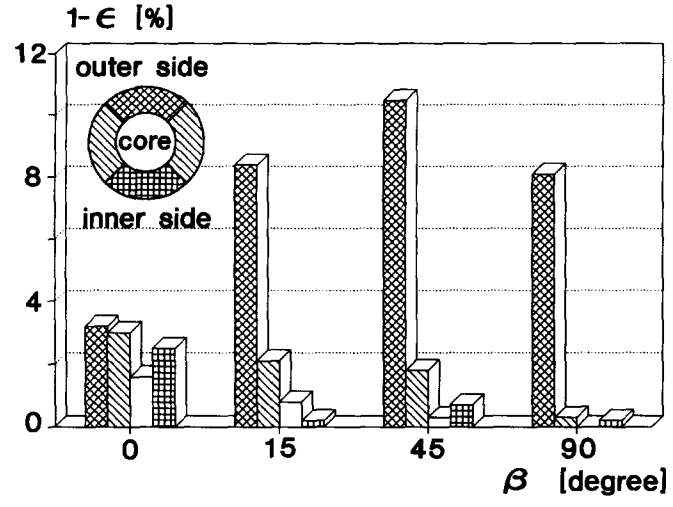


b) measurement of phase distribution

Figure 10. Dispersed flow under non-rewetting status: $R_c/R = 42$, $G = 680\ \text{kg/m}^2$, $\dot{q}_w = 50\ \text{kW/m}^2$, $x_{e,0} = 0.86$, $d_0 = 280\ \mu\text{m}$.

the surface, the thermal repelling forces do not have a comparable magnitude with the centrifugal forces to prevent droplet contact with the wall. Therefore, droplet–wall interactions may be especially important to the wall heat transfer in the bend. In addition, it is interesting to observe different motions of droplets after their first impact on the wall. For droplets of 100 $\mu$m, the secondary flow near the wall is large enough to drive the rebounded droplets towards the inside of the bend. For droplets over 250 $\mu$m, however, the centrifugal effect governs the whole process of impact and rebound. Although these droplets with high impinging Weber numbers break up on the wall, the satellite pieces from the broken bodies are still found to migrate towards the symmetric plane of the bend due to their high tangential momentum.

### *3.3. Phase distribution*

Based on the previous analysis on bulk vapor flow and droplet dynamics, experimental results of phase distribution are examined in this section. To assist discussion, inlet flow conditions

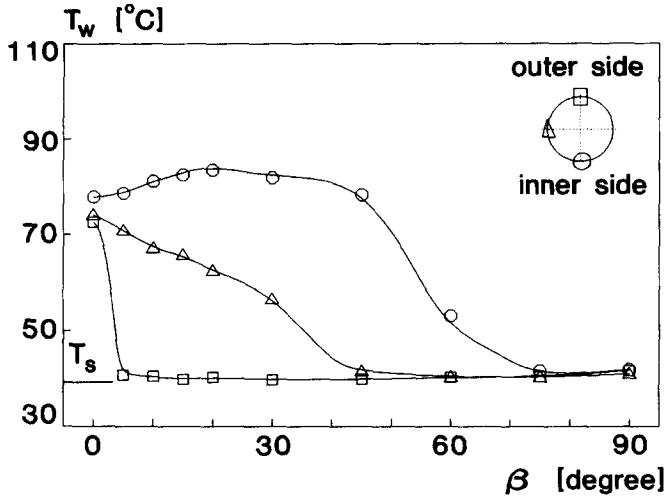


a) measurement of wall temperature

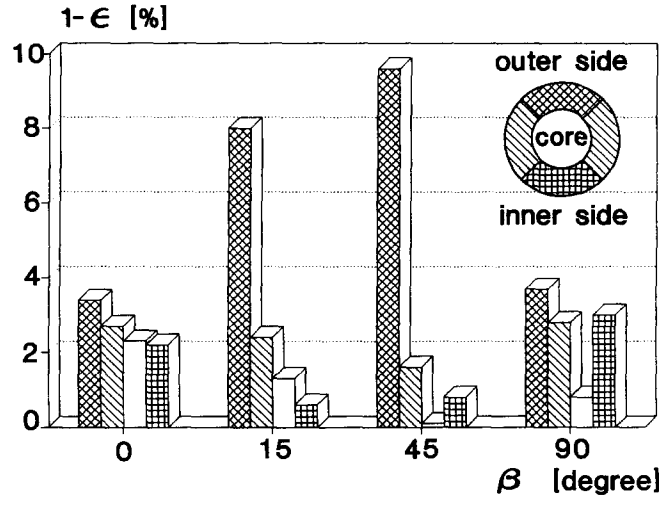


b) measurement of phase distribution

Figure 11. Dispersed flow under rewetting status: $R_c/R = 42$, $G = 1240\ \text{kg/m}^2$, $\dot{q}_w = 30\ \text{kW/m}^2$, $x_{e,0} = 0.81$, $d_0 = 130\ \mu\text{m}$.

(subscript with "0"), e.g. droplet size, vapor quality and velocity of each phase were determined by a one-dimensional heat transfer model (Wang 1993).

Figure 10 shows a typical pattern of the dispersed flow, usually observed under small to median mass fluxes and median to high heat fluxes. Under these conditions, film boiling is maintained [figure 10(a)] and flow structure is characterized by a non-symmetric pattern with most droplets accumulating at the outside of the bend [figure 10(b)]. It is found that the process of phase separation due to differing phasic momentum and body forces begins at the bend inlet, develops further in the early part of the bend and reaches a maximum at about a 45-degree bend angle. According to the above analysis of drop dynamics, this phenomenon is apparently due to the behavior of large droplets associated with the flow, which tend to stay at the outer region. Beginning from the middle of the bend, a decrease in liquid concentration is found in the outer region, attributed to the local evaporation and the droplet inward reversal. The latter effect,

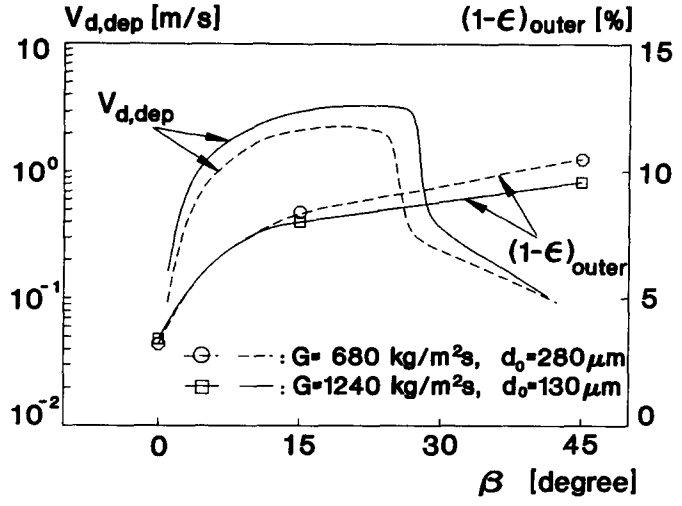


Figure 12. Analysis of droplet deposition rate under the conditions of figures 10 and 11.

confirmed by a slight increase in liquid concentration in the inner region, is active only for those small droplets, which can be transported by the secondary flow. As a result of droplet evaporation, the liquid fraction is reduced overall near the bend outlet.

Figure 11 presents another typical pattern of dispersed flow, usually observed under median to large mass fluxes and small to median heat fluxes. Under these conditions, film boiling is maintained only partially, and rewetting appears firstly on the outer wall, then spreads to the inner wall after some axial distance [figure 11(a)], leading to a complicated flow structure [figure 11(b)]. In the early part of the bend, dispersed flow exhibits a similar pattern of phase distribution as in figure 10(b). Along the second half of the bend, liquid redistribution is observed: the local liquid fraction reduces about 100% in the outer region whereas it increases over 100% in the side and inner regions. Liquid fraction in the core region, however, remains small. According to our theoretical analysis on the droplet motion, it appears impossible for so many droplets to be transported to the inside. Obviously, there is another mechanism responsible for the liquid transportation, namely, liquid film transportation, implied in figure 11(a). To clarify the origin of liquid film formation, the deposition process corresponding to the conditions in figures 10 and 11 is studied in detail in figure 12. It is seen that while the magnitudes of the local liquid concentration in the outer region are nearly the same, the deposition velocity corresponding to the condition in figure 11 is significantly larger than

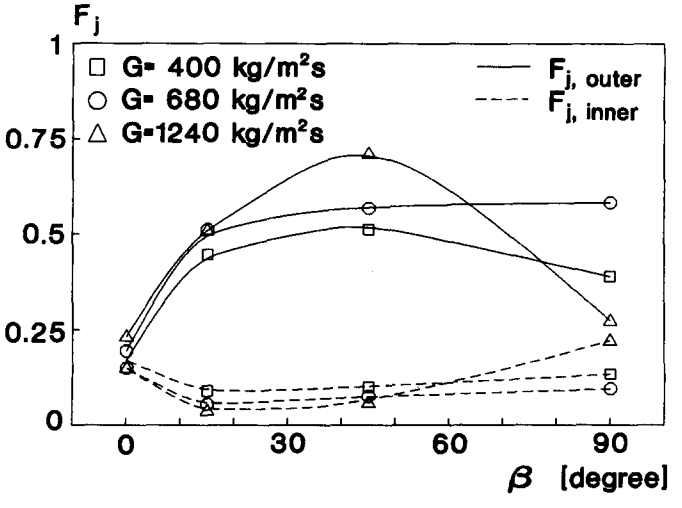


Figure 13. Effect of mass flux on the phase distribution: $R_c/R = 42$, $\dot{q}_w = 30\ \mathrm{kW/m^2}$.

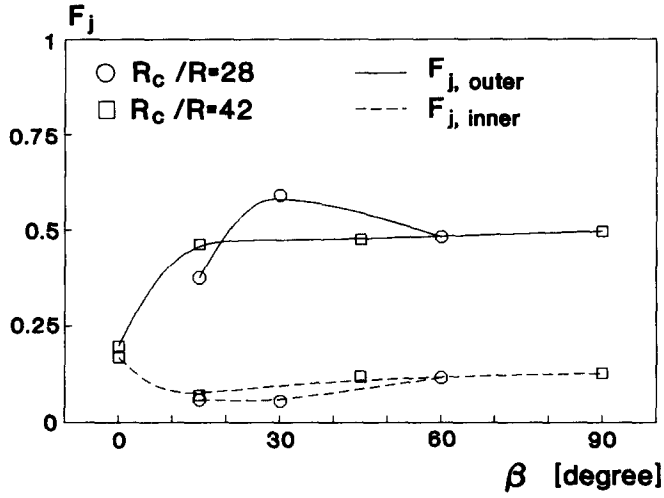


Figure 14. Effect of curvature ratio on the phase distribution: $G = 680\ \text{kg/m}^2$, $\dot{q}_w = 20\ \text{kW/m}^2$.

in figure 10. Therefore the droplet deposition flux in figure 11 is much higher. This leads to a fast quenching of the bend wall where a rewetting condition is established. Consequently, liquid film formed by individual droplets is efficiently transported towards the inner side of the bend under the actions of gravity and interfacial shear stress.

In the following, the effects of several important parameters, i.e. mass flux, curvature ratio and heat flux, on the phase distribution are discussed further. For a quantitative description of phase separation and redistribution, a phase distribution factor $F_j$ is introduced. It is defined as the ratio of liquid volume measured in the local region $j$ to the total liquid volume measured in all five regions of the cross-section

$$F_j = \frac{(1-\epsilon)_j A_j}{\Sigma_k (1-\epsilon)_k A_k} \qquad [25]$$

where $A_k$ is the area of local region $k$. The phase distribution factors in the outer and in the inner region of the cross-section which are studied are of the most interest.

*3.3.1. Effect of mass flux.* Figure 13 presents phase distributions under different mass fluxes. It is seen that phase separation develops rapidly at all three mass fluxes in the first 15 degrees from the bend inlet. A continuous accumulation of liquid in the outer region is found even in the middle

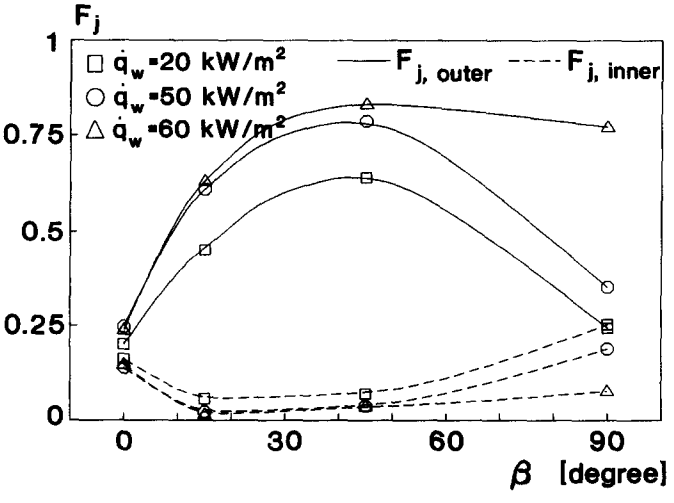


Figure 15. Effect of wall heat flux on the phase distribution: $R_c/R = 42$, $G = 1240\ \text{kg/m}^2$.

of the bend at the mass flux of 1240 kg/m$^2$s. Since a larger mass flux in post-dryout flow corresponds to a smaller droplet size and a larger mean velocity, the phenomenon revealed here indicates clearly the importance of droplet size to the phase separation. Further downstream, a circumferential transportation of liquid from the outer to the inner region is clearly observed at this mass flux due to rewetting discussed above. For the other two mass fluxes, flow structure is dominated only by phase separation whereas phase redistribution in the form of liquid inward reversal is less significant.

*3.3.2. Effect of curvature.* Figure 14 shows phase distributions in two bends of different bend-to-tube radius ratios under the same operational conditions. As indicated in our numerical analysis, a decrease in the bend radius results in an increase in the centrifugal acceleration and the secondary flow. Reflected on the flow structure, the former effects lead to a stronger phase separation in the early part of the smaller radius bend. Once droplets enter the wall region of this bend, the latter effect becomes important, and droplets are more easily transported towards the inside. Consequently, liquid inward reversal is found much faster in the smaller radius bend than in the larger radius bend.

*3.3.3. Effect of heat flux.* Figure 15 presents phase distributions under different wall heat fluxes. It is seen that the dispersed flow structure exhibits similar features when the wall heat flux varies from 20 to 50 kW/m$^2$. In these cases, rewetting appears on the bend wall and liquid transportation is observed in the circumference of the cross-section: liquid concentration keeps decreasing in the outer region and increasing in the inner region. At the highest wall heat flux of 60 kW/m$^2$, however, the amount of heat removed by droplet collisions is no longer large enough to quench the wall below the Leidenfrost point. Under this wall condition, droplets, typically around 160 $\mu$m, evaporate gradually either in the outer region or on their way to the inner region. As a result, phase distribution changes slightly in the latter part of the bend. Thus, wall heat flux is important to the dispersed flow structure only when it changes the heat transfer pattern.

## 4. CONCLUSIONS

Three important aspects of the post-dryout dispersed flow in 90-degree circular bends have been investigated theoretically and experimentally. The theoretical study highlights the details of bulk vapor flow and droplet dynamics under turbulent and thermal effects. The experimental study explores the intricate nature of phase distribution. The results are summarized as follows.

Numerical simulation of the vapor fields reveals some interesting features of the secondary flow. It is found that the secondary flow in two-vortex form develops early in the bend, maintains a maximum region from a 15- to a 45-degree bend angle, and then decreases gradually in the second half of the bend. This implies that the secondary flow may become important to droplet dynamics and phase distribution before the middle of the bend. It is further revealed that the secondary flow in terms of the non-dimensional velocity is less influenced by the change of the bulk Reynolds number. However, it increases significantly with decreases in the bend-to-tube radius ratio.

A Lagrangian droplet trajectory model is developed to study droplet interactions with the turbulent vapor stream and the heated wall. It is shown that droplets reveal a general trend of migration towards the outside of the bend. Under the action of the centrifugal forces droplets may overcome the thermal repelling effect and impinge directly on the hot surface, thus contributing greatly to the wall heat transfer. The effects of the secondary flow and turbulent dispersion are found to bring about a better circumferential transportation of liquid, especially those small droplets. It should be mentioned that the present model does not consider the effect of droplet presence on the vapor fields. The process of droplet collision on the heated wall may be more complicated than the model assumes. Further improvement of the model in these directions is needed in order to allow for a direct comparison of the theory with the two-phase experiments.

Extensive measurements of phase distribution using an impedance probe reveal two different patterns of the dispersed flow. One pattern associated with film boiling is characterized mainly by phase separation, through which most droplets accumulate in the outer region. Once droplet–wall interactions are strong enough to quench the wall below the Leidenfrost temperature, rewetting occurs and dispersed flow reveals another pattern. It is found that the flow structure is firstly

dominated by phase separation and then governed by phase redistribution in the form of liquid inward reversal. Parametric study indicates that increases in mass flux and decreases in bend-to-tube radius ratio lead to a remarkable phase separation and redistribution whereas wall heat flux is important to phase distribution only when it changes the heat transfer pattern.

## REFERENCES

BERGER, S. A., TALBOT, L. & YAO, L.-S. 1983 Flow in curved pipes. *A. Rev. Fluid Mech.* **15,** 461–512.

BOLLE, L. & MOUREAU, J. C. 1982 Spay cooling of hot surface. In *Multiphase Science and Technology* (Edited by HEWITT, G. F. *et al.*), Vol. 1, pp. 1–98. Hemisphere, Washington, DC.

BURNS, A. D. & WILKES, N. S. 1987 A finite difference method for the computation of flows in complex three-dimensional geometries. UKAEA Report No. AERE-R12342.

CHEN, J. C. 1986 A short review of dispersed flow heat transfer in post-dryout boiling. *Nucl. Engng Des.* **95,** 375–383.

CIMORELLI, L. & EVANGELISTI, R. 1967 The application of the capacitance method for void fraction measurement in the bulk boiling conditions. *Int. J. Heat Mass Transfer* **10,** 277–288.

CUMO, M., FARELLO, G. E. & FERRARI, G. 1972 The influence of curvature in post-dryout heat transfer. *Int. J. Heat Mass Transfer* **15,** 2045–2062.

GANIC, E. N. & ROHSENOW, W. M. 1979 On the mechanism of liquid drop deposition in two-phase dispersed flow. *J. Heat Transfer* **101,** 288–294.

GOSMAN, A. D. & IOANNIDES, E. 1981 Aspects of computer simulation of liquid fueled combustors. AIAA Paper No. 81-0323.

LAUTENSCHLAGER, G. 1988 Wärmeübergang in Krümmern bei Sprühkühlung. Dissertation, Technische Universität München, Germany.

LIN, T. F., JOU, J. F. & HWANG, C. H. 1989 Turbulent forced convection heat transfer in two-phase evaporating droplet flow through a vertical pipe. *Int. J. Multiphase Flow* **15,** 997–1009.

MAXWELL, L. 1873 *A Treatise on Electricity and Magnetism.* Oxford University Press, Oxford.

MAYINGER, F. 1982 *Strömung und Wärmeübertragung in Gas-Flüssigkeits-Gemischen.* Springer, Wien.

MAYINGER, F. & LANGNER, H. 1978 Post-dryout heat transfer. *Proc. 6th Int. Heat Transfer Conference*, Toronto, Canada, Vol. 6, pp. 181–198.

RENKSIZBULUT, M. & YUEN, M. C. 1983 Experimetnal study of droplet evaporation in a high temperature air stream. *J. Heat Transfer* **105,** 384–388.

WACHTERS, L. H. J. & WESTERLING, N. A. J. 1966 The heat transfer from a hot wall to impinging water drops in the spheroidal state. *Chem. Engng Sci.* **21,** 1047–1056.

WANG, M. J. 1993 Phasenverteilung, Sekundärströmung und Wärmeübergang bei Sprühkühlung in Krümmern. Dissertation, Technische Universität München, Germany.

WHITE, B. R. 1986 Particle dynamics in two-phase flows. In *Encyclopedia of Fluid Mechanics* (Edited by CHEREMISINOFF, N. P.), Vol. 4, Chap. 8, pp. 240–283. Gulf, Houston, TX.